remote sensing

MDPI

Article

Fine Calibration Method for Laser Altimeter Pointing and Ranging Based on Dense Control Points

Chaopeng Xu [1,2], Fan Mo [2,*], Xiao Wang [3], Xiaomeng Yang [1,2], Junfeng Xie [2] and Zhen Wen [1,2]

1 College of Geodesy and Geomatics, Shandong University of Science and Technology, Qingdao 266590, China; 202182020040@sdust.edu.cn (C.X.); 202082020046@sdust.edu.cn (X.Y.); 202081020010@sdust.edu.cn (Z.W.)
2 Land Satellite Remote Sensing Application Center, Ministry of Natural Resources of China, Beijing 100048, China; xiejf@lasac.cn
3 Aerospace Information Research Institute, Chinese Academy of Sciences, Beijing 100101, China; wangxiao@aircas.ac.cn
* Correspondence: mof@lasac.cn

Abstract: Satellite laser altimetry technology, a novel space remote sensing technique, actively acquires high-precision elevation information about the Earth's surface. However, the accuracy of laser altimetry can be compromised by alterations in the satellite-ground environment, thermal dynamics, and cosmic radiation. These factors may induce subtle variations in the installation and internal structure of the spaceborne laser altimeter on the satellite platform, diminishing measurement precision. In-orbit calibration is thus essential to enhancing the precision of laser altimetry. Through collaborative calculations between satellite and ground stations, we can derive correction parameters for laser pointing and ranging, substantially improving the accuracy of satellite laser altimetry. This paper introduces a sophisticated calibration method for laser altimeter pointing and ranging that utilizes dense control points. The approach interpolates discrete ground control point data into continuous simulated terrain using empirical Bayesian kriging, subsequently categorizing the data for either pointing or ranging calibration according to their respective functions. Following this, a series of calibration experiments are conducted, prioritizing "pointing" followed by "ranging" and continuing until the variation in the ranging calibration results falls below a predefined threshold. We employed experimental data from ground control points (GCPs) in Xinjiang and Inner Mongolia, China, to calibrate the GaoFen-7 (GF-7) satellite Beam 2 laser altimeter as per the outlined method. The calibration outcomes were then benchmarked against those gleaned from infrared laser detector calibration, revealing disparities of 1.12 s in the pointing angle and 2 cm in the ranging correction value. Post validation with ground control points, the measurement accuracy was refined to 0.15 m. The experiments confirm that the proposed calibration method offers accuracy comparable to that of infrared laser detector calibration and can facilitate the updating of 1:10,000 topographic maps utilizing stereo optical imagery. Furthermore, this method is more cost-effective and demands fewer personnel for ground control point collection, enhancing resource efficiency compared to traditional infrared laser detector calibration. The proposed approach surpasses terrain-matching limitations when calibrating laser ranging parameters and presents a viable solution for achieving frequent and high-precision in-orbit calibration of laser altimetry satellites.

Keywords: GF-7; laser altimetry calibration; satellite laser

Citation: Xu, C.; Mo, F.; Wang, X.; Yang, X.; Xie, J.; Wen, Z. Fine Calibration Method for Laser Altimeter Pointing and Ranging Based on Dense Control Points. *Remote Sens.* **2024**, *16*, 611. https://doi.org/10.3390/rs16040611

Academic Editor: Riccardo Roncella

Received: 22 December 2023
Revised: 3 February 2024
Accepted: 5 February 2024
Published: 6 February 2024

1. Introduction

Laser altimetry technology, a potent active remote sensing method [1], has made considerable progress across diverse domains, including surveying and mapping [2], river and lake research [3], oceanography [4], polar glacier observation [5], and planetary exploration [6], attributed to its superior measurement precision and exceptional spatial and temporal resolution. Nevertheless, the emission and operational phases of laser altimeters may be subject to disturbances from vibration, abrupt shifts in the orbital environment, and environmental thermal fluctuations [7]. Such disturbances can lead to modifications in the pointing angle and ranging capabilities of laser altimeters, substantially impacting the accurate pinpointing of the laser footprint's position on the Earth's surface. Research indicates that for terrain with a 1° incline, a 30 s deviation in the pointing of a laser altimeter from an altitude of 600 km can result in horizontal displacements as large as 87 m and vertical inaccuracies up to 1.5 m. The presence of laser ranging errors could exacerbate this discrepancy, potentially exceeding 2 m [8]. Consequently, the geometric calibration of laser altimeters is imperative for curtailing pointing and ranging errors, thereby elevating the fidelity of satellite laser altimetry data.

In the field of geometric calibration of laser altimeters, numerous scholars have conducted rigorous research. Magruder et al. developed a calibration method utilizing laser infrared detectors, which involves deploying a substantial number of these detectors on the ground to capture the footprint of the satellite laser altimetry [9–11]. The centroid of this footprint serves as a ground control point for calibrating the laser altimeter's pointing and ranging [12]. This technique offers the highest accuracy for laser pointing and ranging calibration, and its results are commonly used as a benchmark to validate alternative calibration methods. Luthcke and associates employed a satellite attitude excitation method for calibrating laser altimeters [13–15], which produced commendable results. However, this method is not suitable for satellites equipped with multiple instruments, such as the GaoFen-7 (GF-7), which includes a stereo mapping camera. Liu et al. utilized a waveform-matching approach to calibrate laser altimeters by aligning the emitted laser waveform with the waveform reflected from the actual terrain [16,17]. Tang and associates introduced a laser altimetry satellite pointing calibration method reliant on terrain matching that does not require ground-based instruments and leverages digital surface model (DSM) data for calibrating the laser altimeter's pointing [18]. Xie and team improved the efficiency of this method by implementing a pyramid optimization strategy [19]. Zhao et al. designed a novel terrain-matching technique specifically for estimating systematic biases in pointing and ranging for spaceborne photon-counting laser altimeters [20]. This method, tailored to the attributes of the Ice, Cloud, and land Elevation Satellite-2 (ICESat-2) satellite, calibrates the laser altimeter by matching its ranging profiles with anticipated profiles derived from a robust model. Liu et al. adopted a calibration approach that distinguished between laser pointing and ranging for the GF-7 satellite, using terrain matching to calibrate ranging errors [21]. Nonetheless, this method is contingent on the laser footprint being located on a solid, flat surface, such as an airport runway or a highway.

In the realm of geometric calibration for laser altimeters, current methodologies are unable to satisfy the stringent high-frequency and high-precision in-orbit calibration demands of laser altimetry satellites [22]. Consequently, this paper introduces an advanced calibration method for spaceborne laser altimeter pointing and ranging that utilizes dense control points. Initially, the positions of laser footprints are identified based on their distribution within the designated pointing and ranging calibration areas. Ground control point data, centered around these laser footprints, are collected, and the discrete points are integrated into continuous simulated surface data via empirical Bayesian kriging. These data are subsequently categorized into two sets: one for pointing calibration and another for ranging calibration, tailored to their respective functions. Following this, a sequence of calibration experiments is conducted, adhering to a strategic "pointing-ranging" order. The pointing calibration is undertaken first to ascertain the precision of the laser altimeter's directional pointing, followed by the ranging calibration to enhance the accuracy of the laser range measurements. It is important to note that this series of experiments is iterative rather than a single-step process. Specifically, the ranging calibration is repeated until the variation in the adjusted laser ranging value post calibration is $\leq$0.001 m. This paper employs the GF-7 satellite laser altimeter as the experimental subject and validates the proposed method by drawing comparisons with the calibration results obtained using laser infrared detectors, which are accepted as the reference standard for the GF-7 laser altimeter in this investigation.

Section 2 of this paper outlines the laser data and study area, elucidating the research process and the principal methods applied. Section 3 details the calibration results achieved using the proposed method and substantiates these findings. Section 4 examines the method's practicality for the initial calibration subsequent to satellite deployment, while Section 5 offers a conclusive summary of the research conducted.

2. Materials and Methods

2.1. Study Area and Data

2.1.1. GF-7 Laser Altimeter Data

In November 2019, China successfully launched the GaoFen-7 (GF-7) satellite, marking a milestone as China's first sub-meter-level stereoscopic mapping satellite. Its primary use is for updating large-scale, 1:10,000-scale stereoscopic maps and geographic information data [23,24]. The GF-7 satellite is equipped with a dual-beam laser emission system, with each beam emitting at a wavelength of 1064 nm and a standard frequency of 3 Hz. To enhance the likelihood of capturing ground laser footprints, the measurement frequency of the GF-7 laser altimeter is increased to 6 Hz during the calibration period. Table 1 enumerates select parameters of the GF-7 satellite. For comprehensive details on the hardware parameters and specifications, refer to the work by Xie et al. [25].

Table 1. Basic design parameters of the GF-7 laser altimeter.

Parameter	Value
Number of beams	2
Laser wavelength	1064 nm
Laser energy	100~180 mJ
Emission pulse width	4~8 ns
Laser divergence angle	30~40 μrad
Receiving telescope aperture	600 mm
Pulse repetition frequency	3/6 Hz
Echo digitization interval	0.5 ns
Laser emission efficiency	0.994
Laser receiving efficiency	0.790
Laser ranging range	450~550 km
Laser ranging accuracy	$\leq$0.3 m

Figure 1 illustrates the configuration of the GF-7 spaceborne laser altimeter system. This system employs a dual-beam setup, with a separation angle of 0.7° between the lowest points of the two beams [26]. The laser beams generate 30 m diameter spots on the Earth's surface, with the continuous spots being 2.4 km apart. Additionally, the two beams diverge by approximately 12.25 km across the track direction. The Laser Footprint Camera (LFC) also takes images of the laser footprints and corresponding surface features during laser operations [27]. These images, measuring 1.6 km $\times$ 1.6 km, help establish the geometric relationship between the laser footprints and the line-array stereoscopic mapping camera.

For this research, data from the GF-7 satellite beam 2, collected on 11 and 12 September 2023 over the calibration areas of Kuche in Xinjiang and Xilinguole in Inner Mongolia, were used for laser pointing and ranging calibration. Furthermore, data collected on 23 September 2023 over the Hulunbuir region in Inner Mongolia served as validation data. Figures 2a and 3a depict the specific locations of these two tracks within their respective areas. The particulars of these laser datasets are presented in Table 2. Given the proximity of the dates, it is highly unlikely that there would be any significant changes in the laser altimeter's pointing and ranging parameters, allowing us to assume consistency in the correction parameters for both tracks.

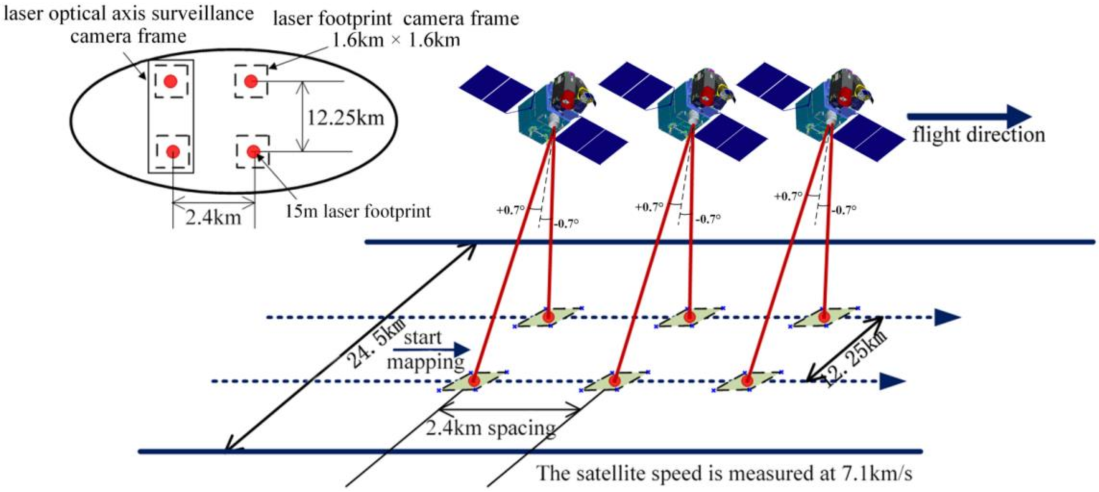

Figure 1. Schematic diagram of the GF-7 spaceborne laser altimeter system.

10	305984093.888

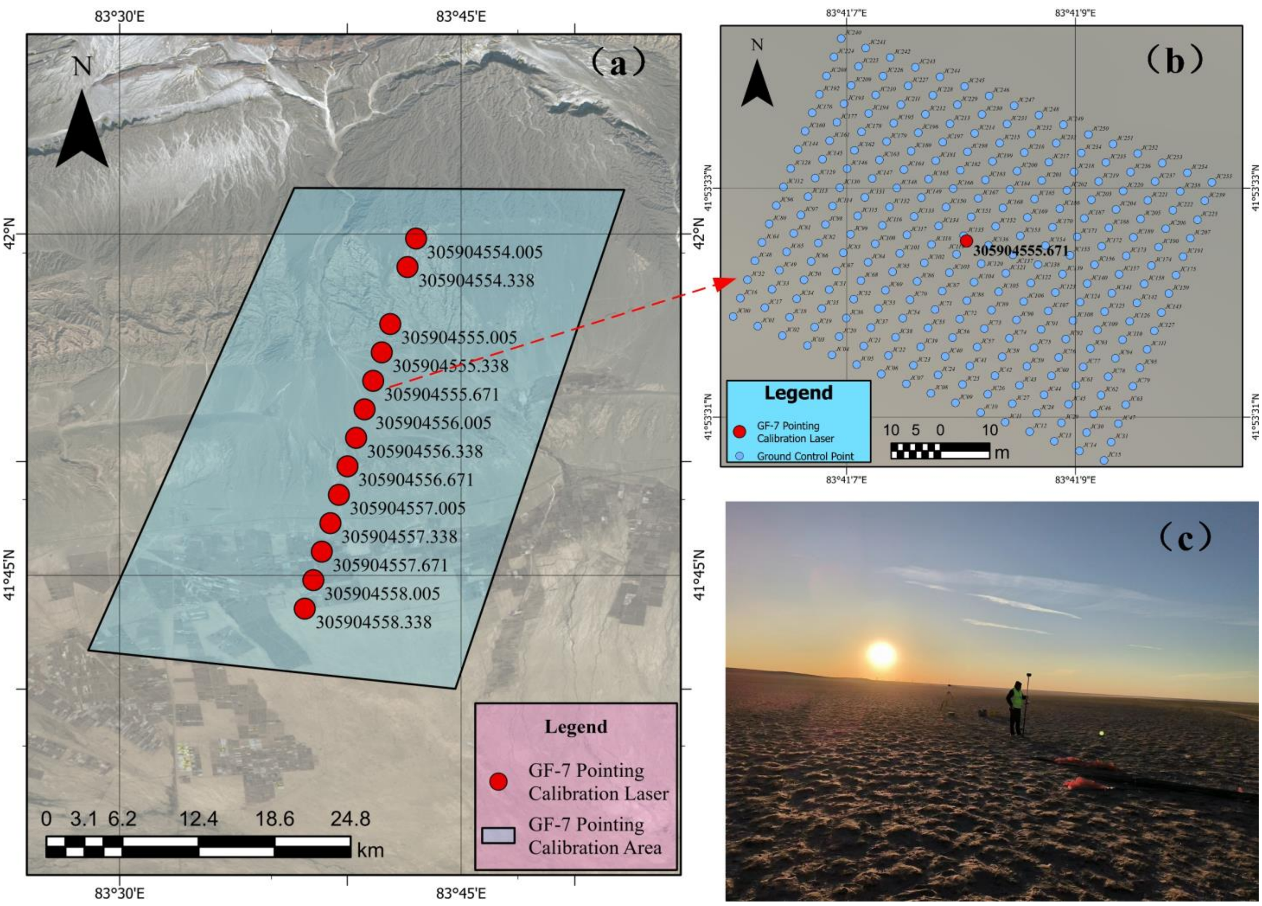

Figure 2. Laser pointing calibration area and laser point data. (**a**) shows the laser pointing calibration area and GF-7 pointing calibration laser data. (**b**) shows the layout scheme of a dense control point grid centered around laser footprint 305904555.671. (**c**) is a map of control point data collection using RTK in the Xinjiang region.

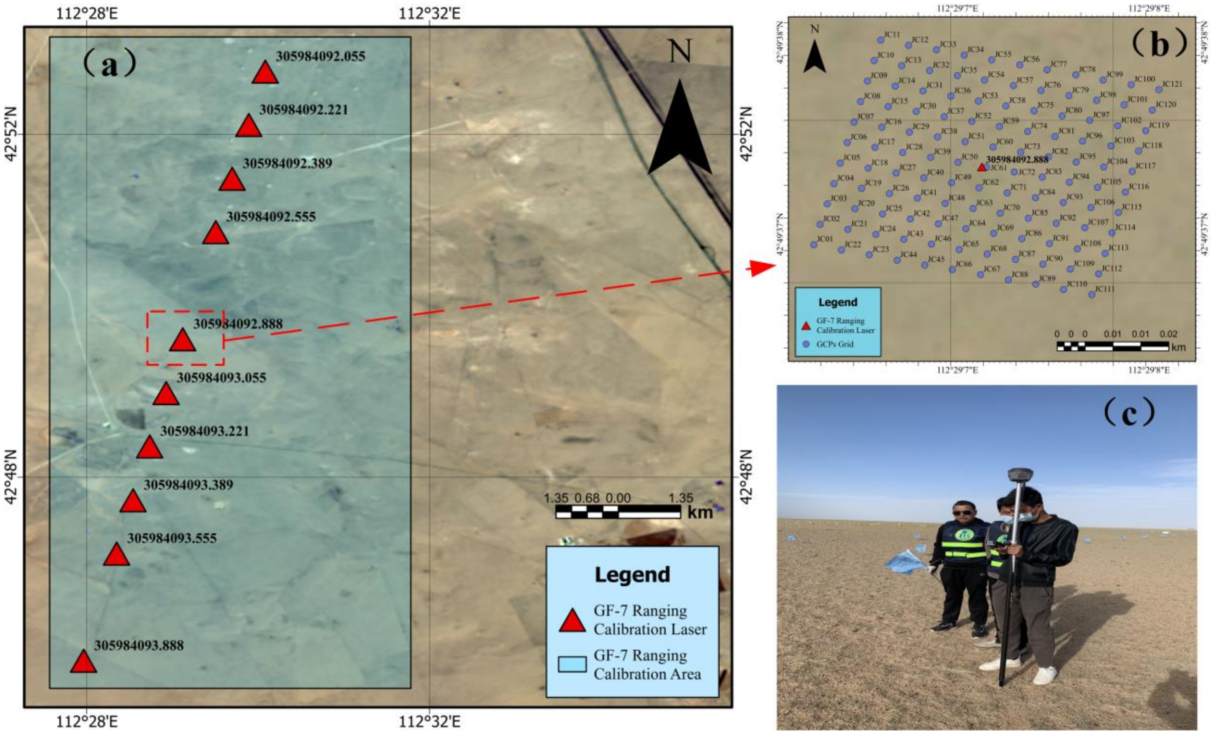

Figure 3. Ranging calibration area and laser footprint locations for GF-7. (**a**) shows the location of the calibration area and the distribution of laser calibration data. (**b**) shows the distribution of ground control point data centered around laser footprint 305984092.888. (**c**) is a picture of ground control point data collection using RTK.

Table 2. GF-7 satellite laser data.

Purpose	Date	Index	Time Code
Pointing Calibration Data	11 September 2023	1	305904554.005
		2	305904554.338
		3	305904555.005
		4	305904555.338
		5	305904555.671
		6	305904556.005
		7	305904556.338
		8	305904556.671
		9	305904557.005
		10	305904557.338
		11	305904557.671
		12	305904558.005
		13	305904558.338
Ranging Calibration Data	12 September 2023	1	305984092.055
		2	305984092.221
		3	305984092.389
		4	305984092.555
		5	305984092.888
		6	305984093.055
		7	305984093.221
		8	305984093.389
		9	305984093.555
		10	305984093.888

2.1.2. GF-7 Laser Altimeter Pointing Calibration Area and Data

The pointing calibration study area for the GF-7 laser altimeter is situated in the mountainous terrain of northeastern Kuche, Xinjiang, as shown in Figure 2a. This area is defined by coordinates ranging from 41.67°N to 42.03°N and from 83.48°E to 83.87°E, encompassing approximately 1158 km^2. Characterized by substantial topographic relief, the region is largely composed of mountains. The arid climate contributes to a landscape dominated by exposed rock, with minimal tall vegetation or man-made structures. These distinctive geographical features and the low level of human activity make this area an ideal location for conducting the laser altimeter pointing calibration study. Environmental stability, which is largely unaffected by anthropogenic or natural alterations, is essential for obtaining accurate pointing calibration results.

On 11 September 2023, during its 21,914th orbit, the GF-7 satellite laser altimeter passed over the designated pointing calibration area. Following the post-processing of the laser data, a total of 13 laser footprints were identified within the calibration area. These footprints served as central points for establishing a control point grid, as depicted in Figure 2b. This grid has a square configuration, each side measuring 60 m in length, with a 4 m interval between control points. The coordinates for each control point were determined using Real-Time Kinematic (RTK) positioning [28], achieving an elevation accuracy of up to 0.05 m. The control point grid collection approach for all 13 laser footprints was consistent with the pattern shown in Figure 2b for footprint 305904555.671. Figure 2c depicts the collection of control point data using RTK.

2.1.3. Ranging Calibration Area and Data for Laser Altimeter

The laser altimeter's ranging calibration study area, as presented in this paper, is situated within a specific section of the Xilingol League in the Inner Mongolia Autonomous Region of China, as shown in Figure 3a. The geographical coordinates for this region span from 42.75°N to 42.89°N and from 112.46°E to 112.53°E, covering an area of approximately 80.38 km^2. The dominant landscape feature is the Gobi Desert, known for its level terrain, which substantially aids in the positioning and gathering of ground control point data. The selection of this terrain for our study is predicated on its suitability for the environmental conditions required for ranging calibration. The Gobi Desert's characteristics ensure precise measurements and clear identification of control points, while the flat terrain streamlines the measurement process and enhances the efficiency of data collection. These attributes provide a compelling rationale for selecting this location for the ranging calibration efforts.

On 12 September 2023, during the GF-7 satellite's 21,927th orbit, the laser altimeter data traversed the ranging calibration area. Post-processing of this data revealed a total of 10 laser footprints within the calibration zone. Two days later, on September 14th, ground control point data were collected in the calibration area. At the site, we set up a specific grid pattern surrounding the identified laser footprints, as illustrated in Figure 3b. This grid also has a square structure, with each side measuring 40 m and a 4 m separation between the control points. The grid's coordinate information was acquired using RTK positioning, ensuring the elevation accuracy was maintained at up to 0.05 m. Figure 3b displays the control point grid centered on the laser footprint with the time code 305984092.888. The grid layout for additional laser footprints was identical. The availability of high-precision ground control point data lays a robust foundation for the accurate ranging calibration of the GF-7 satellite's spaceborne laser altimeter. Figure 3c depicts the collection of ground data within a calibration area using RTK.

2.2. Overall Process

The methodology of this paper is illustrated in Figure 4 and encompasses five distinct steps:

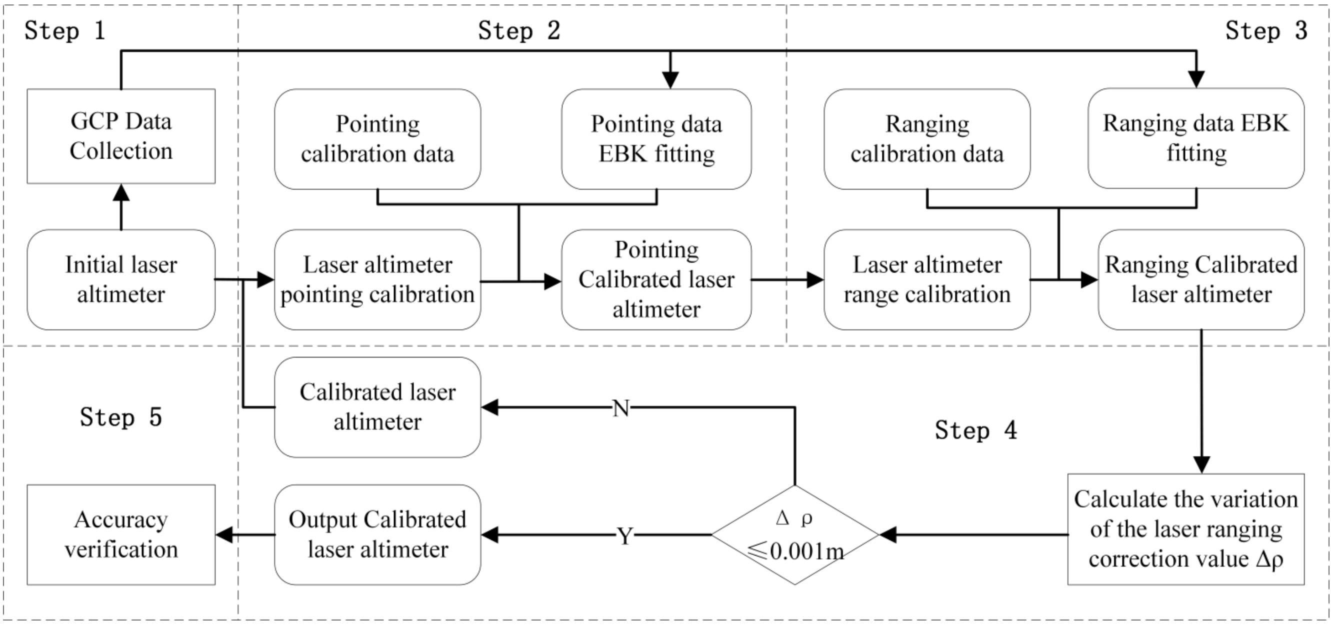

Figure 4. Laser altimeter calibration process flowchart.

Step 1: Simulated Surface Fitting Based on Ground Control Points (GCPs)

In orbit, the pointing parameters of the satellite laser altimeter remain relatively stable. Leveraging the calibration parameters from 2022 as a starting point, we position the laser ranging calibration data and collect GCPs centered on the identified laser footprint locations. We then fit the discrete GCP data into a digital surface model using the empirical Bayesian kriging method, which provides the terrain reference necessary for the calibration of the laser altimeter's ranging capabilities.

Step 2: Laser Altimeter Pointing Calibration

We commence the pointing calibration of the laser altimeter using the installation parameters or previously established calibration parameters as a baseline, in conjunction with the finely simulated digital surface model as the reference terrain. Initially, we generate a set of potential pointing angles centered around the initial values. Subsequently, we compute the root-mean-square error (RMSE) between the measured laser elevation data and the corresponding values from the finely simulated surface for each angle. The optimal pointing angle for calibration is selected based on the angle that yields the minimum RMSE.

Step 3: Laser Altimeter Ranging Calibration

With the laser altimeter parameters derived from the pointing calibration as our input and the finely simulated digital surface model as our reference terrain, we proceed to the ranging calibration. We first determine the positions of the laser points using the laser footprint positioning model. The next step involves calculating the elevation discrepancies between each laser point and the corresponding reference terrain data. These differences are then applied within the laser altimeter ranging calibration equation to ascertain the necessary ranging correction values.

Step 4: Iterative Calculation

Upon completion of the ranging calibration, we examine the change in the ranging correction value ($\Delta\rho$). If $\Delta\rho \geq 0.001$ m, the parameters from this iteration are retained as the initial parameters for a new cycle of pointing and ranging calibration, starting again at Step 2. This iterative process continues until $\Delta\rho \leq 0.001$ m.

Step 5: Calibration Results Verification

To verify the accuracy of the laser altimeter's pointing and ranging parameters calibrated through this paper, we utilize the parameters obtained from the calibration conducted using a ground-based infrared laser detector as the benchmark. GCP coordinates that correspond to the calibrated laser footprint locations are collected via RTK. The elevation accuracy of these calibrated laser footprints is then validated using the GCP data.

2.3. Methods

2.3.1. Laser Altimeter Pointing Calibration

Laser pointing error is often the primary contributor to geolocation discrepancies and is a significant cause of horizontal positioning inaccuracies [29–31]. It also plays a crucial role in the introduction of elevation errors, particularly in areas with moderate-to-steep slopes. The procedure of calibrating the pointing of a spaceborne laser altimeter can be visualized using a simplified two-dimensional illustration, as shown in Figure 5.

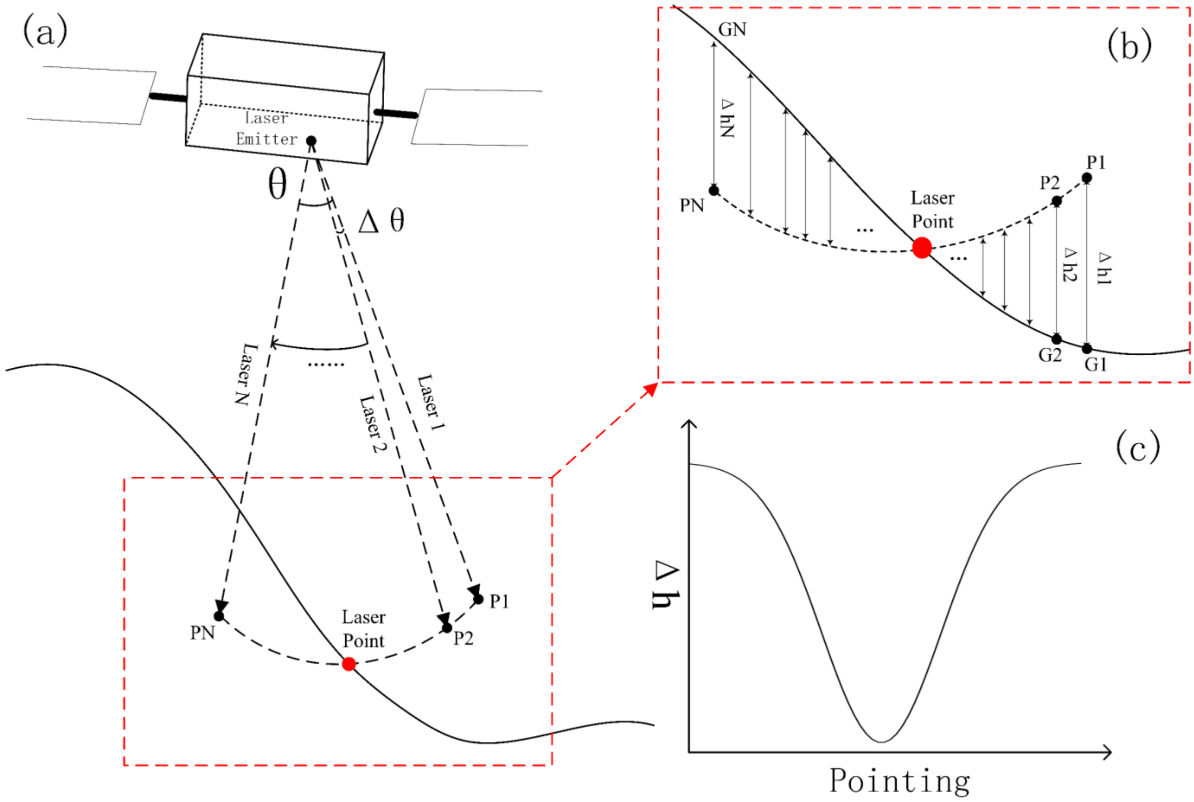

Figure 5. Laser altimeter pointing calibration geometry. (**a**) illustrates the process of laser altimeter pointing calibration in a two-dimensional image. (**b**) shows the elevation differences between the laser footprints from different pointing positions and the ground elevation. (**c**) depicts the relationship between ideal laser pointing and elevation differences.

In Figure 5a, θ represents the range of pointing calibration and $\Delta\theta$ denotes represents the angular difference between adjacent pointing angles during calibration. Laser 1, Laser 2, . . ., Laser N represent lasers emitted at different pointing angles under the same ranging conditions. P1, P2, . . ., PN represent the positions of laser footprints located at different pointing angles. The diagram depicts that the pointing positions P1 and PN are obtained by setting the initial pointing angle to $\pm\frac{\theta}{2}$. Within this range, different pointing angles are obtained at intervals of $\Delta\theta$. Subsequently, a total of N pointing positions are obtained. The positions P1 to PN can be calculated after locating the laser footprints.

In Figure 5b, P1, P2, . . ., PN represent the positions of laser footprints located at different pointing angles. G1, G2, . . ., GN denote the ground locations corresponding to the latitude and longitude of the located laser footprints. $\Delta h1$, $\Delta h2$, $\ldots \Delta hN$, express the elevation differences between the laser footprint positions and the corresponding ground points for different pointing positions.

In Figure 5c, we see a plot that demonstrates the relationship between various laser pointing angles and the absolute elevation discrepancies they produce. There is a noticeable trend showing a set of pointing angles at which the absolute difference in elevation between the laser footprint and the actual ground point is minimized, creating a pronounced "funnel" effect on the graph. Typically, the angle associated with this minimum absolute elevation difference is selected as the calibrated pointing angle.

The scenario described is an idealized version of the pointing calibration process. In reality, the calibration can be influenced by factors such as the complexity of terrain variations, laser ranging errors, and anomalies in ranging measurements. Occasionally, elevation differences for certain laser points may be anomalous, and selecting the pointing angle with the smallest absolute elevation difference may not lead to the most accurate result. To mitigate this, the root-mean-square error (RMSE) is employed as a more robust metric to evaluate the precision of various pointing angles, taking the place of the absolute elevation difference.

$$\begin{cases} Index = \min\left(\sqrt{\frac{1}{N}\sum_{i=1}^{N}\left(h_{Point_i} - h_{Groud_i}\right)^2}\right) \\ P_{Optimal} = P_{index}, P = \{pointing_1, pointing_2, \ldots, pointing_N\} \end{cases} \tag{1}$$

where h_{Point_i} represents the elevation of the i-th laser footprint position, h_{Groud_i} represents the elevation of the corresponding ground point for the i-th position, Index represents the index of the optimal pointing angle, $pointing_i$ represents the i-th pointing angle, P represents the set of all pointing angles, and $P_{Optimal}$ represents the calibrated optimal pointing angle.

When discussing the parameters of a laser altimeter's pointing, we describe its orientation using the zenith and azimuth angles. As depicted in Figure 6a, we define a Cartesian coordinate system with the laser emitter at the origin and the z-axis extending perpendicularly from the ground. The azimuth angle is determined from the x-axis direction. In Figure 6a, α denotes the azimuth angle, while β indicates the zenith angle.

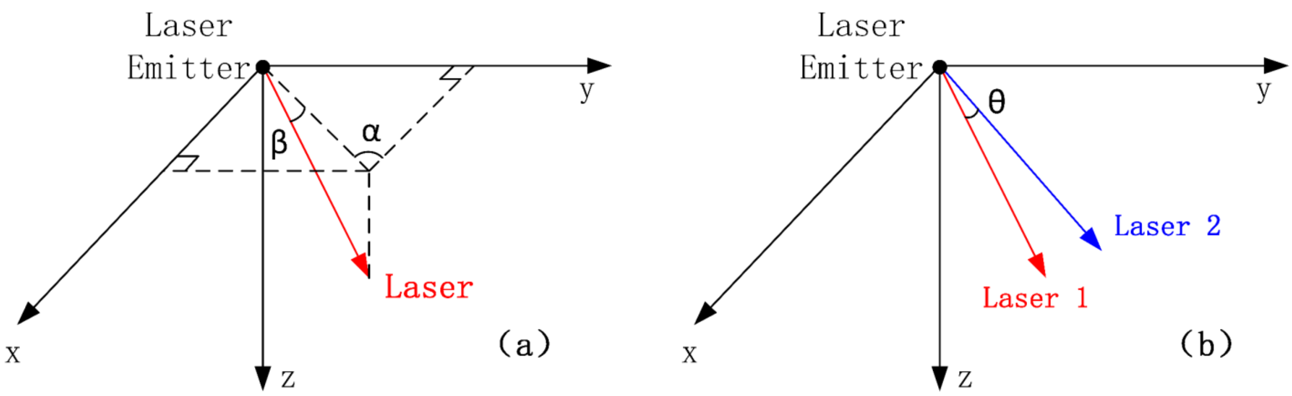

Figure 6. The geometric structure of the relevant parameters for the laser altimeter. (**a**) shows a schematic representation of laser pointing using zenith and azimuth angles. (**b**) depicts the spatial angles between different laser pointings.

It is important to acknowledge that α and β are two physical quantities that precisely characterize the laser's pointing direction. However, when validating the accuracy of the pointing calibration, it is possible to encounter situations where one physical quantity shows improved precision at the expense of the other's accuracy when comparing different calibration methods. To resolve this, we introduce the concept of spatial angles as a comprehensive metric to evaluate the accuracy of pointing calibration. In Figure 6b, θ is the spatial angle between Laser 1 and Laser 2. The formula for calculating θ is as follows:

$$\theta = \arccos(sin\beta_1 sin\beta_2 + cos\beta_1 cos\beta_2 cos(\alpha_1 - \alpha_2)) \tag{2}$$

In the formula, α_1, β_1 represent the laser pointing of Laser 1; α_2, β_2 represent the laser pointing of Laser 2; and θ represents the spatial angle between Laser 1 and Laser 2. The magnitude of the spatial angle reflects the degree of deviation between the two laser pointings.

2.3.2. Simulation Surface Fitting Based on Empirical Bayesian Kriging (EBK)

Empirical Bayesian kriging (EBK) offers significant benefits in the fitting of simulated surface data derived from ground control points, particularly when working with control point sets structured on 40 m × 40 m or 60 m × 60 m grids with 4 m intervals. EBK enhances the classical kriging method's spatial interpolation capabilities by incorporating Bayesian statistical optimization, yielding an efficient and adaptive method for spatial interpolation [32–34]. A key strength of EBK is its automated optimization of the semivariogram function parameters. The semivariogram function, γ(h), delineates the relationship between the spatial interval, h, of the data points and the sample semivariance—a critical factor for interpolation precision. Using a Bayesian framework, EBK automatically estimates these parameters by maximizing the likelihood function, or posterior probability, to refine the interpolation model. The foundational formula can be represented as follows:

$$Z^*(s_0) = \mu + \sum_{i=1}^{n} \lambda_i (Z(s_i) - \mu) \tag{3}$$

where $Z^*(s_0)$ is the predicted value at location s_0, $Z(s_i)$ is the observed value at the known location s_i, μ is the global mean, and λ_i are the weight coefficients determined by minimizing the variance of the prediction error.

In the context of fitting simulated surface data with GCPs, spatial data commonly display considerable heterogeneity and intricacy. EBK meets this challenge head-on by auto-adjusting the semivariogram function. Unlike traditional kriging methods, which necessitate manual selection and fine-tuning of the semivariogram by the user—a task that can be daunting in complex terrains and with irregular sampling—EBK simplifies this process, thereby reducing the user's burden and elevating the model's adaptability and precision. Furthermore, EBK excels at managing sparse or irregularly distributed control point data. By simulating the uncertainty of the semivariogram function, it provides confidence intervals for the interpolated values, ensuring the reliability of the interpolation outcomes even when faced with substantial intervals between data points.

Consequently, empirical Bayesian kriging presents an effective and dependable approach for the fitting of simulated surface data using GCPs, especially pertinent in scenarios demanding higher spatial resolution, intricate terrain features, and uneven data distribution. In this paper, EBK has been selected as the fitting method for simulated surface data using a GCP dataset, with the primary goal of calibrating spaceborne laser altimeter parameters. For additional details on this method, please consult the work of Krivoruchko et al. [35–37].

2.3.3. Laser Altimeter Range Calibration

Within this paper, the calibration model for the spaceborne laser altimeter's range measurements is developed by examining the geometric relationship between the calculated laser footprint position and its actual position, informed by inferences drawn from laser ranging errors. Initially, we hypothesize that the laser footprint is situated on a perfectly horizontal surface, enabling us to draft a schematic diagram for laser ranging error analysis as illustrated in Figure 7.

As depicted in the figure, $\rho_{measure}$ represents the laser ranging value used for laser footprint positioning, while ρ_{real} represents the true laser ranging value from the laser transmitter to the ground. $P1$ represents the true position of the laser footprint on the ground, $P2$ denotes the position calculated by the laser footprint positioning model, and $P3$ is a ground point with the same latitude and longitude as $P2$. θ represents the angle between the laser and the vertical line on the ground, including the angle at which the laser transmitter is installed and the satellite yaw angle. ρ_{error} represents the laser ranging error, and its calculation formula satisfies

$$\rho_{error} = \frac{h_{P2} - h_{P3}}{\cos(\theta)}, \tag{4}$$

where h_{P2} and h_{P3} represent the elevation values of $P2$ and $P3$, respectively. h_{P2} is calculated by substituting the laser ranging value $\rho_{measure}$ into the laser footprint positioning model, and h_{P3} is the elevation value of the reference terrain data at the same latitude and longitude.

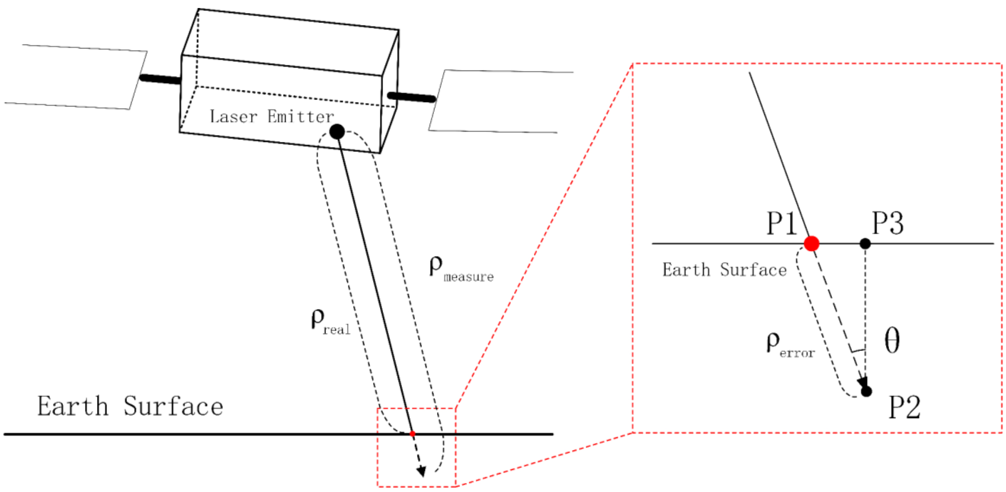

Figure 7. Schematic diagram of laser ranging error analysis.

In theory, the elevation difference should be zero. Nevertheless, for a set of N laser data points, there will be N corresponding laser ranging errors. The discrepancy between these errors and zero represents the systematic error induced by the laser ranging process. To mitigate this error, we select the mean value of these discrepancies as the compensatory figure for the systematic error. This compensation value is attained by tweaking the laser ranging correction value within the input parameters, thereby amending the systematic error. It may also be referred to as the variation in the laser ranging correction value.

Thus, the laser ranging correction value subsequent to the calibration of the laser altimeter range should be the aggregate of the original laser ranging correction value and its subsequent variation. The calculation formula for this correction is as follows:

$$\begin{cases} \Delta o = mean\left(\sum_{i=1}^{N} \rho_{error_i}\right) \\ \rho = \rho_0 + \Delta o \end{cases} \tag{5}$$

where ρ represents the laser ranging correction value after laser ranging calibration, ρ_0 is the laser ranging correction value in the input parameters used for positioning laser ranging data, ρ_{error_i} expresses the ranging error of the i-th laser footprint, and Δo is the variation in the laser ranging correction value and also the condition for stopping the iteration in this experiment.

3. Results

3.1. Laser Altimeter Pointing and Ranging Calibration Results

We performed a laser altimeter pointing calibration experiment with the GF-7 laser altimeter in 2022. The calibration was performed with a range of $\pm 0.05°$ and an interval of $0.000001°$ for the calibration angles. Using the parameters obtained after pointing calibration, we obtained the laser footprint positions for laser ranging calibration. We calculated the variation in the laser ranging correction value and the laser ranging correction value based on the laser altimeter ranging calibration method. The experiment was iterated twice, and the variation in the ranging correction value was found to be 0.001 m, indicating the termination of the iteration. The two iterations of this experiment are presented in Figure 8.

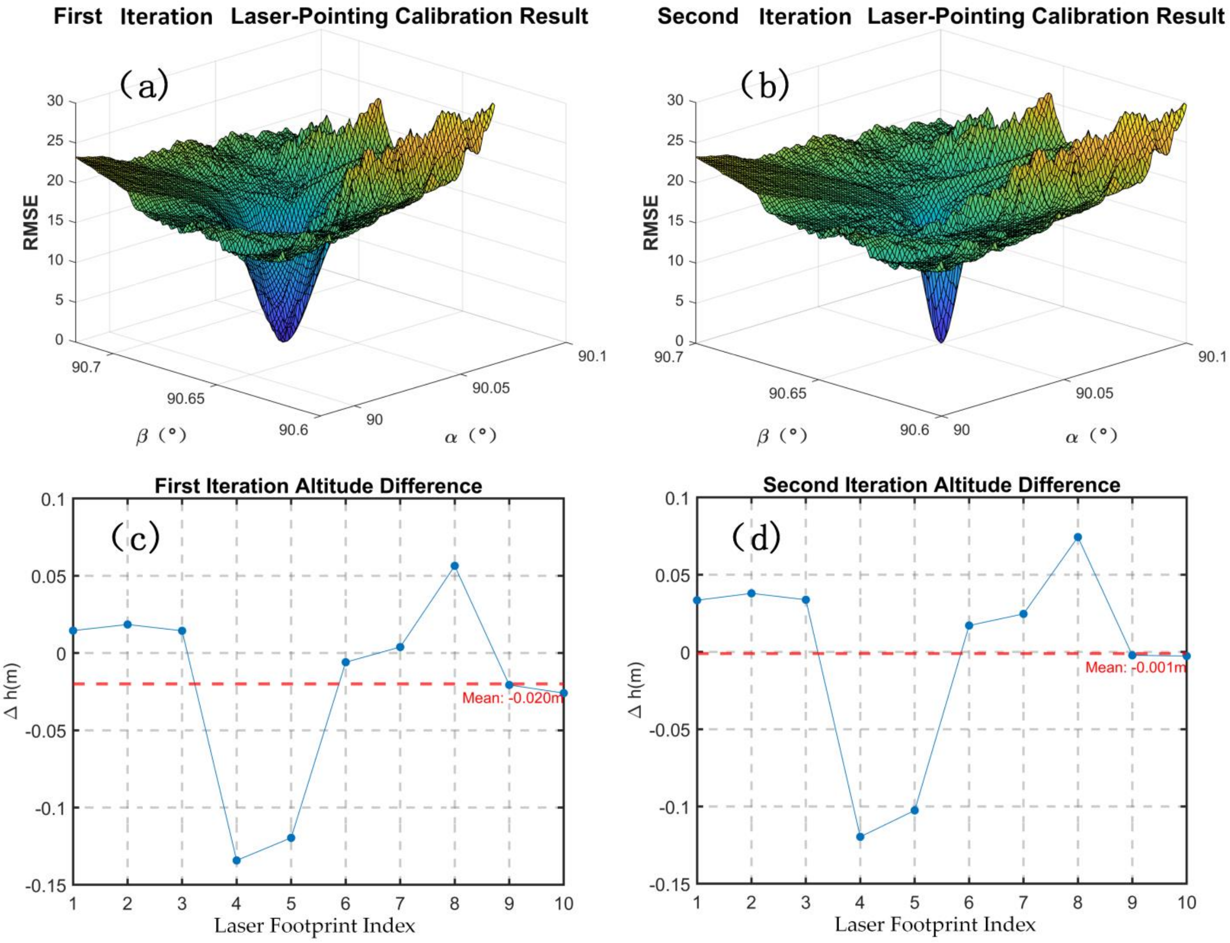

Figure 8. Results of the two iterations of laser altimeter pointing and ranging calibration. (**a**) represents the results of the first iteration of pointing calibration, while (**b**) represents the results of the second iteration of pointing calibration. (**c**) represents the results of the first iteration of ranging calibration, and (**d**) represents the results of the second iteration of ranging calibration. In (**c**,**d**), the blue lines represent the elevation difference at different laser points, and the red dashed lines represent the average elevation difference.

The results of the two iterations of pointing calibration are displayed in Figure 8a,b. It can be clearly seen from the figure that both iterations exhibit a "funnel-shaped" pattern, aligning with the ideal calibration shape, indicating the good performance of the pointing calibration. In Figure 8b, the bottom of the "funnel" is sharper, indicating that after one iteration, the pointing is closer to the true pointing.

The results of the two iterations of ranging calibration are displayed in Figure 8c,d. The horizontal axis represents the laser footprint index, and the vertical axis Δh represents the elevation difference between the laser footprint and the simulated ground data.

After two iterations of calibration, compared to the 2022 laser altimeter parameters (initial parameters), the laser altimeter pointing angle α changed by $-0.000677°$ (2.44 s), the pointing angle β changed by $0.000283°$ (1.02 s), and the laser ranging correction value changed by -0.02 m.

3.2. Validation of Laser Altimeter Calibration Results

The calibration method for spaceborne laser altimeter parameters using laser infrared detectors is recognized for its superior accuracy. Consequently, we adopted the parameters calibrated through this technique as the definitive values to validate the methodology of our research. The crucial aspect of employing this method effectively is the accurate capture of laser footprints. To accomplish this, we positioned laser infrared ground detectors in the Hulunbuir region of Inner Mongolia, China, in accordance with the forecasted orbital path of the GF-7 satellite. The geographical setting of this region is depicted in Figure 9a.

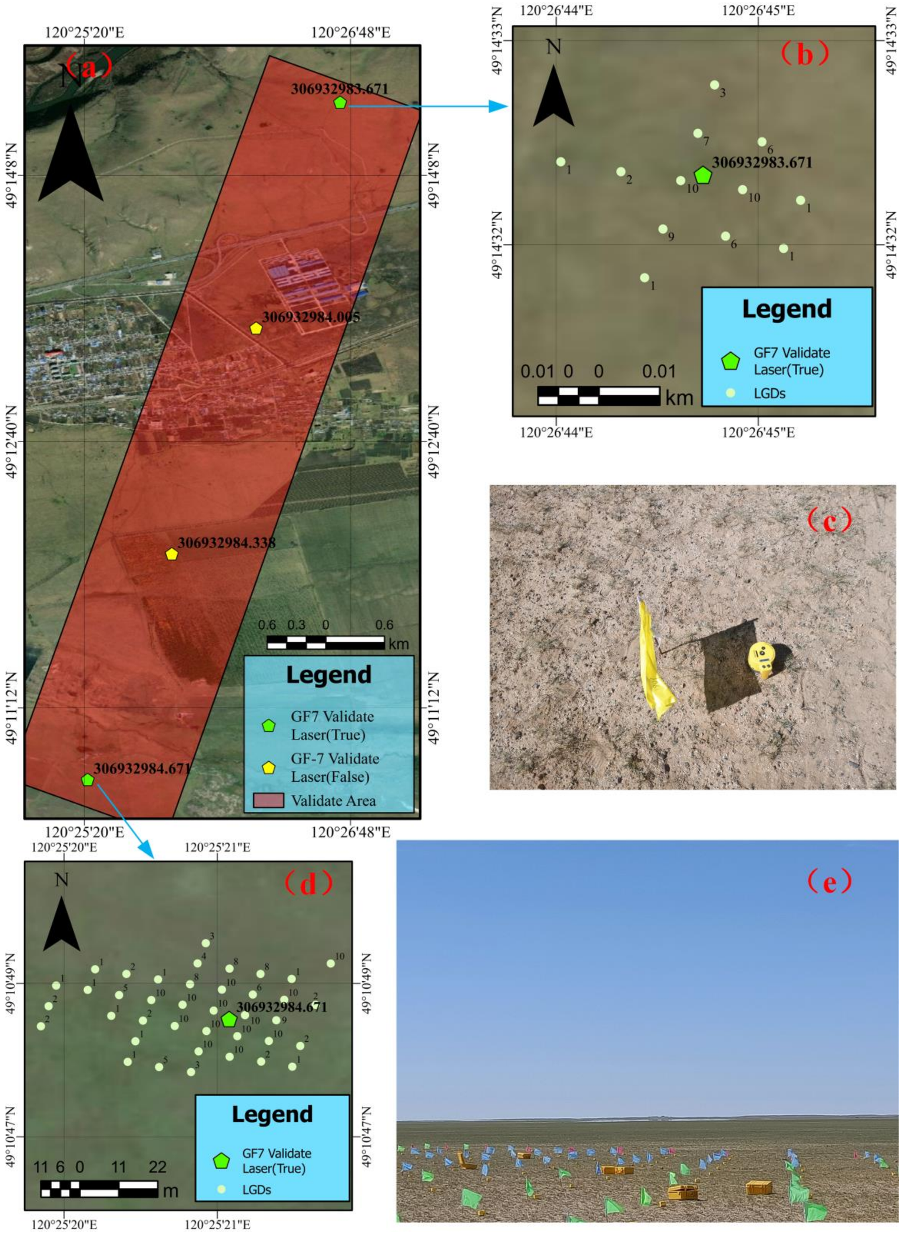

Figure 9. Laser validation area and data. (**a**) displays the laser validation area and the positions of the GF-7 validation laser footprints. The green laser footprints represent successful captures by the detector, while the yellow ones indicate that they were not captured. The red area represents the validation region. (**b**) illustrates the positions of laser footprint 306932983.671 and the detector, with the numerical values indicating the laser trigger energy. (**c**) displays the laser infrared detector used in this experiment. (**d**) shows the positions of laser footprint 306932984.671 and the detector, with the numerical values indicating the laser trigger energy. (**e**) presents a real-life image of the detector deployment in this experiment.

In line with the projected trajectory of the GF-7 satellite, we delineated a rectangular area measuring 7.6 km by 1.2 km, totaling approximately 9.12 km^2. The selected area is predominantly covered by grasslands and barren terrain, characterized by its level ground and absence of tall vegetation or artificial structures that could interfere with the measurements. On the day of the calibration experiment, the conditions were ideal, with clear skies and excellent visibility.

On 23 September 2023, based on the projected path of the GF-7 satellite, it was anticipated that four laser footprints would intersect the designated laser validation area. In preparation, we strategically placed ground laser detectors at the four expected locations. The detectors were arranged in a rectangular grid with 6 m intervals, spanning an area of 36 m $\times$ 48 m. Following the transit of the GF-7 satellite, an inspection of the ground detectors confirmed the successful capture of two satellite laser footprints. However, some detectors experienced malfunctions due to equipment issues. In Figure 9b,d, we have showcased only the positions and energy levels of the detectors that were activated.

For the two accurately captured laser footprints, we employed a technique known as "Centroid Extraction of Laser Spots Captured by Infrared Detectors" [38,39], which integrates laser footprint imagery with detector observational data to precisely determine the centroid positions of the detected laser spots. Figure 10 illustrates the application of this method for pinpointing the centroid positions of the laser footprints. The calibration exercise for the GF-7 satellite's spaceborne laser altimeter parameters, utilizing the ground-based laser detectors, was thus successfully completed.

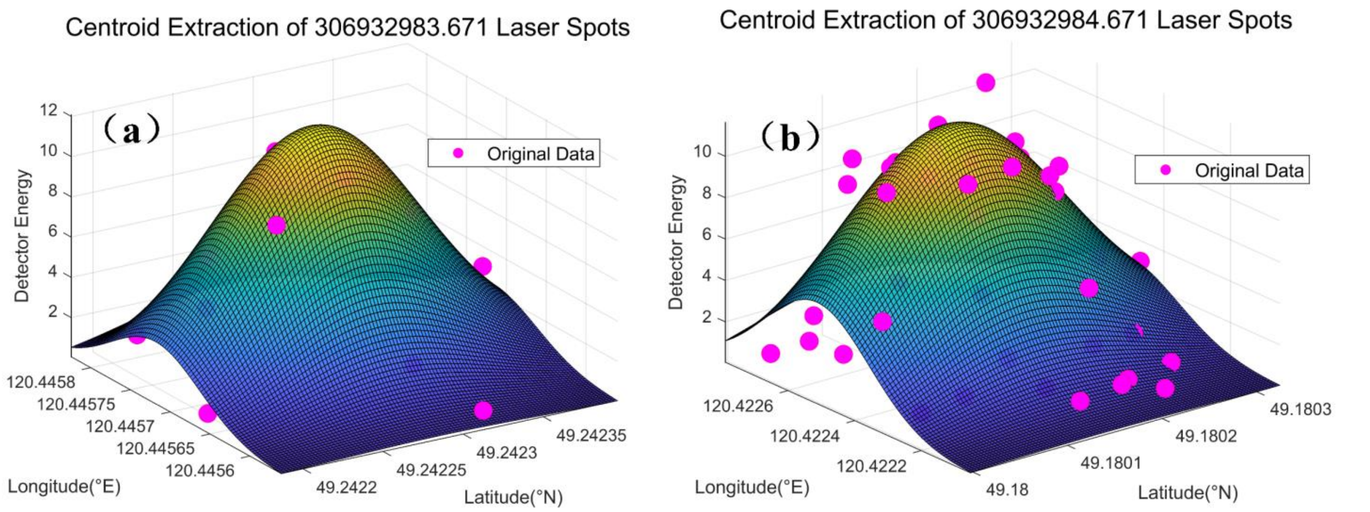

Figure 10. Centroid extraction of ground detectors. (**a**) shows the centroid extraction of the detector that captured laser footprint 306932983.671. (**b**) illustrates the centroid extraction of the detector that captured laser footprint 306932984.671.

We used the calibration outcomes from the detectors as the benchmark parameters for the GF-7 satellite's spaceborne laser altimeter to corroborate the calibration results obtained in this paper. Table 3 lists the initial parameters of the laser altimeter, the parameters after the first and second iterations, and the variances between these parameters and the benchmark values. $\Delta\alpha$ represents the angular difference between the calibrated pointing angle α and the true pointing angle α; $\Delta\beta$ represents the angular difference between the calibrated pointing angle β and the true pointing angle β; and $\Delta\rho$ represents the difference between the calibrated range correction value and the true range correction value. θ represents the angular difference between the calibrated laser direction and the true laser direction.

The validation data in Table 3 reveal that after applying the calibration method described in this paper, there was a notable improvement in the accuracy of the laser altimeter's pointing angles. Specifically, the pointing angle α's accuracy was enhanced from −0.000580° (−2.09 s) to −0.000097° (−0.35 s), while the accuracy of pointing angle β initially decreased from −0.000010° (−0.04 s) to −0.000293° (−1.05 s). Nevertheless, the overall accuracy of the pointing angles improved from 0.00058° (2.09 s) to 0.000314° (1.13 s), which represents an enhancement of 45.93% in accuracy. With a simple estimation that a 1 s deviation in the satellite's pointing at an altitude of 500 km equates to a planar shift of approximately 2.45 m on the Earth's surface, the method improved the planimetric accuracy from an error of 5.12 m to 2.77 m, a 45.9% increase in accuracy. Additionally, the range correction value of the laser altimeter became more precise, improving from −0.04 m to −0.02 m, which equates to a 50% improvement in accuracy.

Table 3. Validation of laser altimeter parameters after calibration using the method described in this paper.

	Δα (°)	**Δβ (°)**	**θ (°)**	**Δρ (m)**
Initial Iteration	−0.000580	−0.000010	0.000580	−0.04
First Iteration	0.000116	−0.000306	0.000333	−0.02
Second Iteration	−0.000097	−0.000293	0.000314	−0.02

Table 4 details the discrepancies in the positions of laser footprints recorded by the ground detectors before and after the application of the calibration method discussed in this paper.

Table 4. Differences between the laser footprint after calibration in this paper and the captured laser footprint.

Time Code	**Δ*Lat* (°)**	**Δ*Lon* (°)**	**Δ*Distance* (m)**	**Δ*h* (m)**
306932983.671	−0.000013	0.000032	2.742	0.017416
306932984.671	−0.000013	0.000032	2.745	0.017422
Mean	−0.000013	0.000032	2.744	0.017419

Table 4 indicates that the laser footprint after calibration in this paper is very close to the laser footprint captured by the ground detector. The latitude difference between the two is −0.000013°, the longitude difference is 0.000032°, the average planar distance difference is 2.744 m, and the average elevation difference is 0.017419 m. The actual validation results align with the rough calculations mentioned earlier.

To verify the elevation accuracy of the laser footprint after calibration in this paper, we re-calibrated the laser altimeter parameters using the method in this paper for the data of orbit 21,914 on 11 September 2023. The distribution of the calibrated laser footprints is depicted in Figure 11. We went to the area and adopted RTK to collect the positions of the initial laser footprint (before calibration with the 2022 laser altimeter parameters) and the calibrated laser footprint (after calibration as per this paper).

From Figure 11, we observe that the planar positions and elevations of the laser footprints exhibit some variation before and after calibration. Nevertheless, these changes are relatively minor, primarily attributable to the slight differences in the spaceborne laser altimeter parameters pre and post calibration. To assess the actual enhancement in elevation accuracy afforded by the methodology proposed in this paper, we validated the elevation of the laser footprints against ground coordinates obtained via RTK surveying. Detailed comparisons of the laser footprint positions before and after calibration, along with the GCP positions acquired by RTK, are presented in Table 5.

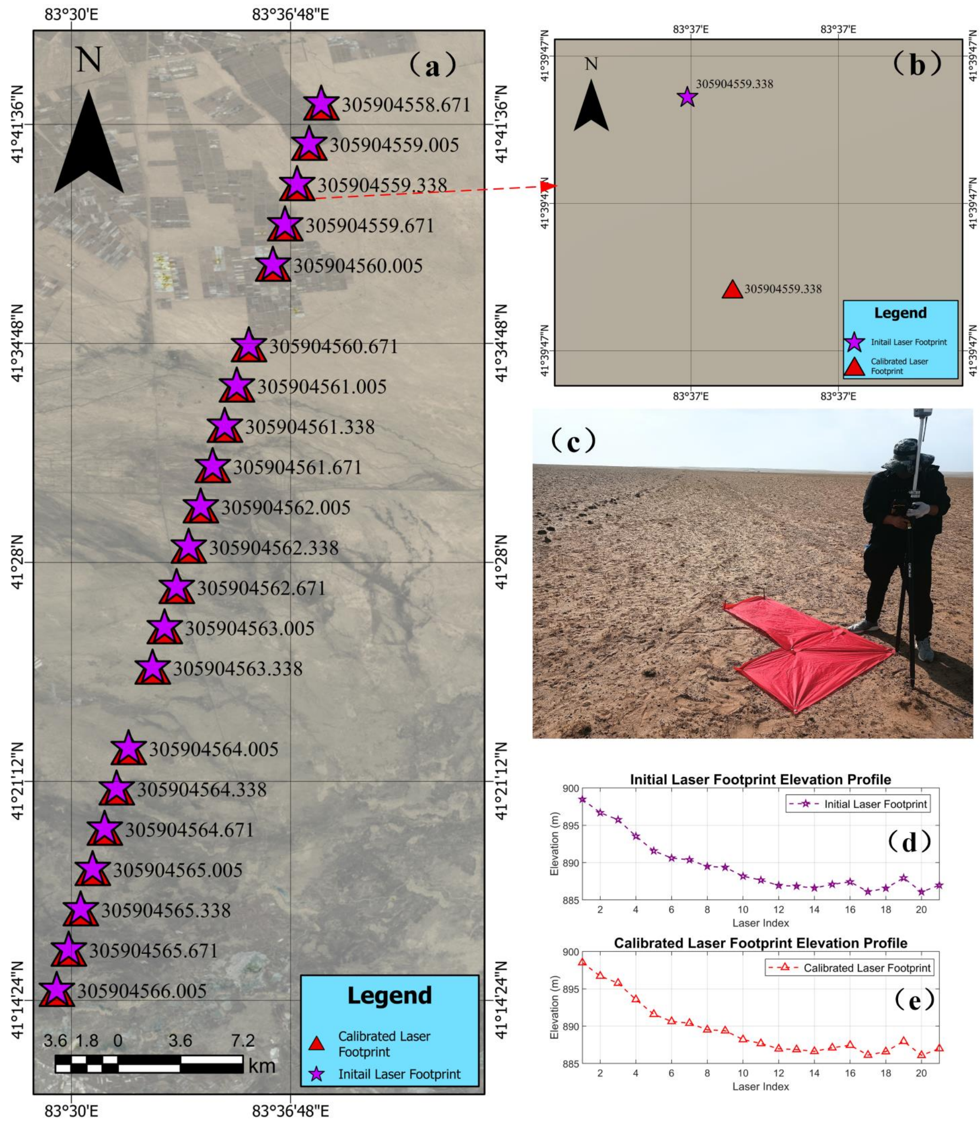

Figure 11. Distribution of elevation-validated laser footprints. (**a**) shows the approximate distribution of the initial laser footprint and the calibrated laser footprint. (**b**) shows the planar positions of the laser footprints before and after the calibration with a value of 305904559.338. (**c**) is a photo taken during the RTK measurement. (**d**,**e**) show the changes in the elevation of the laser footprints before and after calibration.

In the table, the "Initial" column lists the position data of the laser footprints using the original spaceborne laser altimeter parameters (those from 2022). The "Calibration" column contains the position data of the laser footprints post calibration. Latitude (*Lat*), longitude (*Lon*), and altitude (*H*) correspond to the respective coordinates of the laser footprints. "GCP_H" denotes the altitude of the ground control points collected by RTK. The symbol Δh indicates the discrepancy between the altitude of the laser footprints and that of the GCPs. According to Table 5, the average altitude discrepancy between the laser footprints and the GCPs before calibration stood at -0.26 m, with an elevation accuracy of 0.36 m. Following calibration, we notice a marked improvement in elevation accuracy. The average altitude error is reduced from -0.26 m to just -0.01 m, and the elevation accuracy is enhanced from 0.36 m to 0.15 m—translating to a 58.33% increase in precision. Figure 12 illustrates the alterations in the elevations of the laser footprints as a consequence of the calibration process.

Table 5. Elevation validation of laser footprints before and after calibration.

	Index	*Lat* (°)	*Lon* (°)	*H* (m)	GCP_H (m)	Δh (m)	MEAN	RMSE
Initial	1	41.93	83.70	1243.12	1243.34	−0.21	−0.26 m	0.36 m
	2	41.89	83.69	1172.13	1172.79	−0.66		
	3	41.87	83.68	1127.82	1128.10	−0.28		
	4	41.79	83.65	932.71	933.15	−0.44		
	5	41.77	83.65	901.94	902.23	−0.29		
	6	41.75	83.64	901.10	901.12	−0.03		
	7	41.73	83.64	900.04	899.92	0.13		
	8	41.68	83.62	896.68	896.97	−0.28		
	9	41.64	83.61	893.54	893.64	−0.10		
	10	41.58	83.59	890.61	890.78	−0.16		
	11	41.56	83.59	890.37	890.55	−0.17		
	12	41.52	83.57	889.36	889.58	−0.22		
	13	41.50	83.57	888.18	888.33	−0.14		
	14	41.48	83.56	887.66	887.81	−0.15		
	15	41.45	83.55	886.94	887.15	−0.21		
	16	41.37	83.53	887.08	887.33	−0.24		
	17	41.33	83.52	886.10	886.33	−0.23		
	18	41.29	83.50	887.95	888.13	−0.18		
	19	41.27	83.50	886.07	886.33	−0.26		
	20	41.25	83.49	886.97	888.08	−1.11		
Calibration	1	41.93	83.70	1243.15	1243.13	0.01	−0.01 m	0.15 m
	2	41.89	83.69	1172.16	1172.16	−0.01		
	3	41.87	83.68	1127.84	1127.91	−0.07		
	4	41.79	83.65	932.74	932.77	−0.03		
	5	41.77	83.65	901.96	902.15	−0.19		
	6	41.75	83.64	901.12	901.24	−0.12		
	7	41.73	83.64	900.07	899.94	0.12		
	8	41.68	83.62	896.71	896.96	−0.25		
	9	41.64	83.61	893.56	893.64	−0.08		
	10	41.58	83.59	890.64	890.79	−0.15		
	11	41.56	83.59	890.40	890.46	−0.06		
	12	41.52	83.57	889.39	889.61	−0.23		
	13	41.50	83.57	888.21	888.36	−0.15		
	14	41.48	83.56	887.68	887.86	−0.18		
	15	41.45	83.55	886.96	886.93	0.04		
	16	41.37	83.53	887.11	887.28	−0.17		
	17	41.33	83.52	886.13	886.37	−0.24		
	18	41.29	83.50	887.97	888.08	−0.11		
	19	41.27	83.50	886.10	886.32	−0.22		
	20	41.25	83.49	887.00	886.85	0.14		

In Figure 12, the initial laser footprint elevation prior to calibration shows pronounced variability when contrasted with the GCP elevations. The altitude difference ranges from a minimum of −1.11 m to a maximum of 0.13 m, yielding a span of 1.14 m. Post calibration, however, the calibrated laser footprint elevation shows more consistent variations in relation to the GCP elevations. The altitude difference narrows, with the minimum being −0.25 m and the maximum being 0.12 m, culminating in a range of 0.37 m—a significant decrease from the pre-calibration extremities. Additionally, it is evident that the calibrated laser footprint elevations are more closely aligned with zero.

Therefore, based on validations using laser data from orbit 21,914 on 11 September 2023, the calibration method introduced in this paper effectively corrects minor deviations in the spaceborne laser altimeter. These deviations could result from several operational factors, including mechanical jitter, cosmic radiation, and fluctuations in the thermal environment of the satellite. After applying the proposed calibration technique, the difference between the laser altimeter's pointing parameters and the ground detector calibration results narrows to 0.000314° (1.13 s), and the discrepancy in the range correction value parameter is finetuned to 2 cm. The elevation accuracy of the spaceborne laser altimeter, as corroborated using the GCPs, is established at 0.15 m.

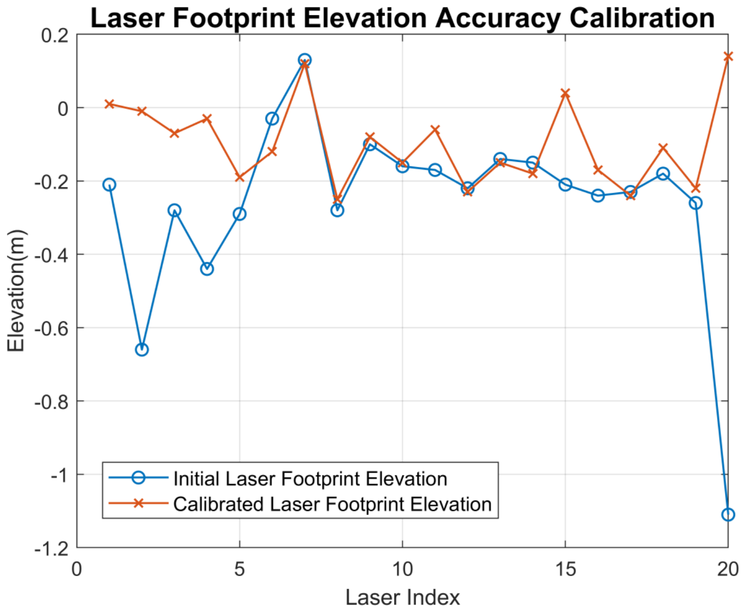

Figure 12. Laser footprint elevation accuracy before and after calibration.

4. Discussion

The calibration of spaceborne laser altimeter parameters can be divided into two distinct phases: the initial calibration following the satellite's launch and the subsequent periodic calibrations carried out during the satellite's operational period. The initial calibration is conducted using the pre-launch ground installation parameters of the laser. However, due to the intense vibrations experienced during launch, there can be notable discrepancies between these initial parameters and the post-launch calibration results. Consequently, prior to the aforementioned calibration process, an initial laser altimeter pointing calibration based on terrain matching is required. This procedure can significantly mitigate the pointing errors of the laser altimeter. In the context of our experimental analysis, we regard this terrain-based pointing calibration as the initial iteration in the calibration sequence.

For the pointing calibration of the laser altimeter, we establish the initial calibration range at ±0.5° around the nominal ground installation pointing angle. The calibration is performed at increments of 0.000001°, and the laser altimeter pointing calibration experiment is subsequently conducted. Following each iteration, the newly acquired parameters are employed for geolocation purposes to ascertain the position of the laser footprint, which in turn facilitates the laser range calibration. The adjustment in the range correction value is computed using the laser altimeter range calibration method. After five iterations, when the adjustment in the range correction value stabilizes at zero, the iterative process is concluded. Figure 13 delineates the outcomes of these five iterations of the pointing calibration, along with the variations in the pointing angles α and β.

Figure 13a represents the first iteration of the pointing calibration. Since the ground installation parameters are employed as the initial parameters applied, a relatively large calibration range of ±0.5° is set for this calibration. In the subsequent calibration process, (b) and (c) have a range of ±0.05°, and (d) and (e) have a range of ±0.005°. The pointing interval is set to 0.000001° for all cases. It can be observed that as the calibration range decreases, the "funnel" shape in the images becomes less sharp. The reason for this finding is that when the calibration range is reduced, the change in RMSE in the images is not as drastic, resulting in smoother images.

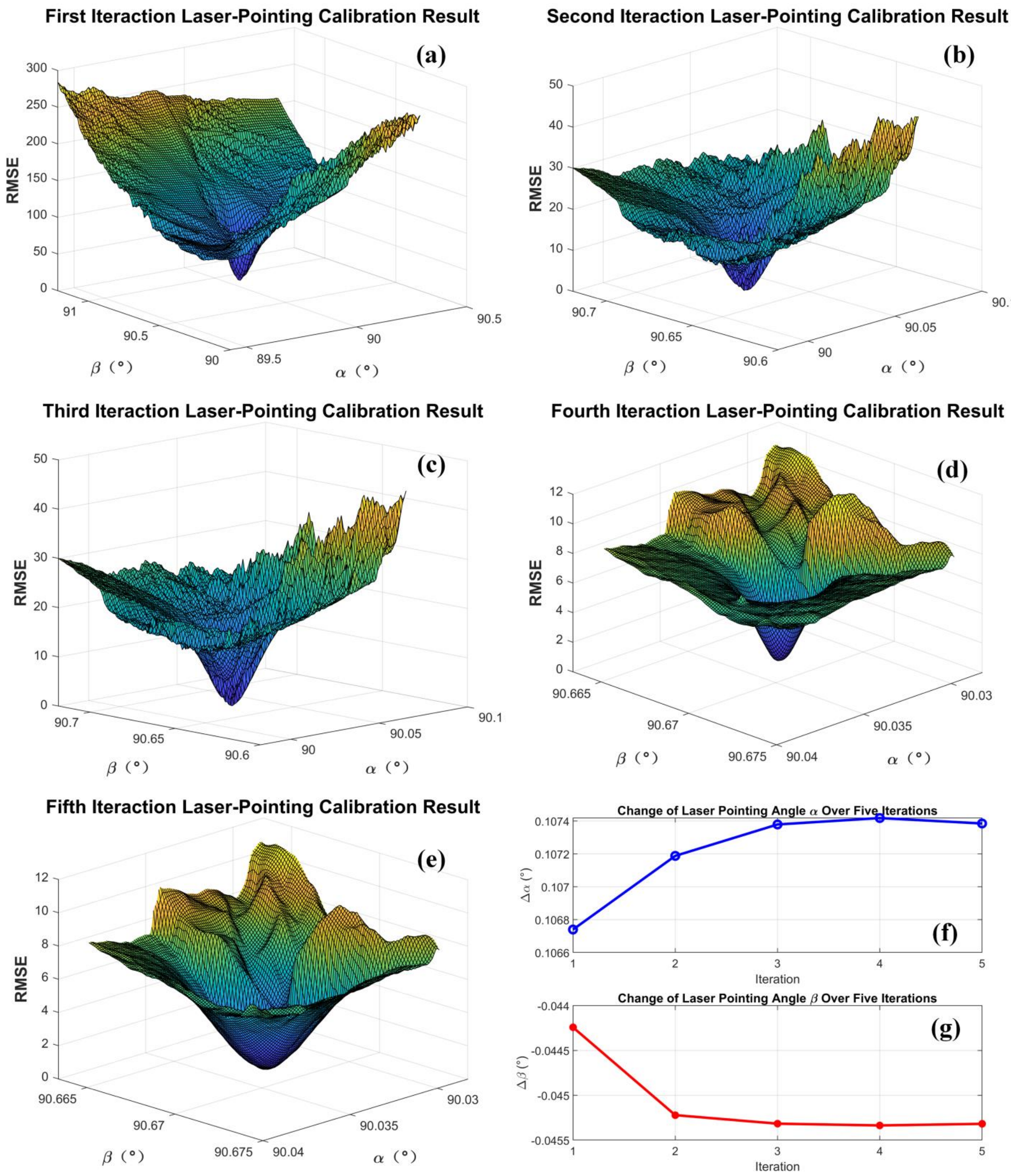

Figure 13. Results of the five iterations of pointing calibration and the variations in the pointing angles α and β. (**a**–**e**) represent the results of the first to fifth iterations of pointing calibration, respectively. (**f**) illustrates the variation in the laser pointing angle α during the five iterations, while (**g**) shows the variation in the laser pointing angle β during the five iterations.

In Figure 13f,g, we show the variations in the calibrated pointing angles α and β relative to the initial pointing angles in the five iterations. In the y axis, $\Delta\alpha$ and $\Delta\beta$ represent the differences from the initial pointing angles α and β, respectively. The pointing angles α and β converge after three iterations, and the converged values vary significantly compared to the initial parameters, thus suggesting a notable difference between the satellite's post launch pointing parameters and the ground installation parameters.

The variations in the differences between the laser footprint elevation and the ground elevation are illustrated in Figure 14 for the five iterations.

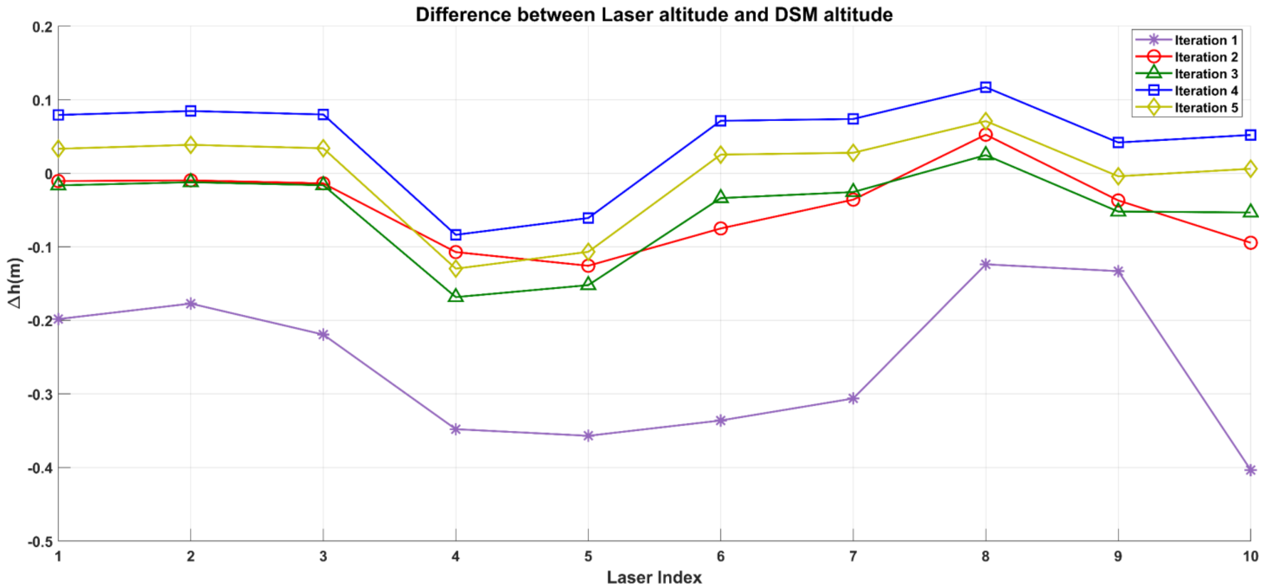

Figure 14. Changes in the differences between the laser footprint and the simulated ground surface elevation during the five iterations.

In Figure 14, Δh represents the elevation difference between the laser footprint and the simulated ground elevation, and Laser Index refers to the ten laser footprints used for laser range calibration. Since the initial range correction value is set to 0, the elevation difference between the laser footprint and the simulated ground is initially large during the first iteration. As the iterations progress, the elevation difference gradually decreases and hovers around 0. Table 6 presents the variations in the laser range correction values for the five iterations.

Table 6. Variations in laser range correction values for the five iterations.

	First Iteration	Second Iteration	Third Iteration	Fourth Iteration	Fifth Iteration
Δo	−0.26 m	−0.046 m	−0.051 m	0.046 m	0 m

The results show a substantial adjustment during the first iteration, attributed to the initial parameter's range correction value starting at zero. Successive iterations witness a marked reduction in the variation in the laser range correction value until it stabilizes at zero in the fifth iteration. This suggests that after five iterations, the discrepancies between the laser footprint positions and the simulated ground surface elevations are symmetrically distributed around zero. Hence, the calibration parameters deduced from the fifth iteration are deemed to be the definitive outcomes.

In a similar vein, we corroborate the calibration results and methodology by juxtaposing them with the calibration outcomes of the laser infrared detector obtained in 2023, which are regarded as the reference standard. Table 7 provides a comprehensive breakdown of the validation results for the calibrated laser altimeter parameters, ensuring the integrity and reliability of the calibration process.

The parameters outlined in Table 7 should be interpreted with reference to Table 3. It is apparent that there were notable differences between the laser altimeter parameters in 2023 and the pre-launch ground installation parameters. Following the satellite's launch, the laser pointing experienced a deviation of 0.115610° (416.2 s). A rough estimate suggests that a 1 s deviation in the satellite's pointing at an operational altitude of 500 km translates to a footprint deviation of approximately 2.5 m on the ground. Consequently, the planimetric positioning accuracy between the 2023 laser altimeter calibration parameters and the initial ground installation parameters exhibited a disparity of over 1 km. This substantial deviation underscores the necessity of executing a pointing calibration before determining the range calibration area. After the first iteration calculation, the satellite's pointing deviation was reduced to 0.001589° (5.72 s), resulting in a planimetric positioning error of around 14.01, which falls comfortably within the 40 m × 40 m grid employed for range calibration.

Table 7. Validation of laser altimeter parameters after calibration.

	$\Delta\alpha$ (°)	$\Delta\beta$ (°)	θ (°)	$\Delta\rho$ (m)
Initial Iteration	0.107480	−0.045610	0.115610	−0.33
First Iteration	0.000740	−0.001368	0.001589	−0.07
Second Iteration	0.000292	−0.000389	0.000498	−0.03
Third Iteration	0.000101	−0.000294	0.000316	0.03
Fourth Iteration	0.000062	−0.000274	0.000284	−0.02
Fifth Iteration	0.000095	−0.000292	0.000314	−0.02

For the GF-7 satellite, we regard the laser altimeter parameters calibrated by the ground detector in 2023 as the benchmark parameters. Subsequent to the calibration performed using the method detailed in this paper, the laser altimeter's pointing angle α showed a minor discrepancy of 0.000095° (0.342 s) when compared to the benchmark, and the pointing angle β differed by −0.000292° (1.05 s), with the cumulative pointing angle deviation being 0.000314° (1.13 s). Given that a 1-arc-second deviation in pointing translates to an approximate planimetric difference of 2.45 m at the satellite's operating altitude of 500 km, the resulting planimetric position discrepancy is about 2.74 m. The laser range correction value differed by 2 cm.

The calibration method proposed in this paper is shown to yield consistent results for both the initial post-launch calibration experiment and the operational calibration of the satellite laser altimeter conducted in 2023. This consistency is logical given that both calibration exercises utilized the same ground reference data, with the primary distinction being the significant differences in the satellite laser altimeter parameters. When the iteration ceases, the position of the laser footprint should ideally align optimally with the ground reference data, which is theoretically unique to that set of reference data. Consequently, the final calibration results for both operational states of the satellite should theoretically converge. Given that the calibrated laser altimeter parameters are identical in both scenarios, it follows that their elevation accuracy would be consistent with the earlier discussed elevation accuracy validation results. For this reason, the elevation accuracy validation for these parameters is not reiterated in this section.

5. Conclusions

This paper introduces an innovative calibration method for laser altimeter pointing and ranging based on dense control points. This method tackles the challenges of correcting systematic errors in laser altimetry satellites over the short term and the scarcity of calibration opportunities. Compared to traditional ground detector calibration techniques, our approach maintains similar accuracy levels while significantly reducing resource needs, showing lower operational complexity and a higher success rate. The effectiveness and precision of the method were validated through comparison with ground detector calibration results, particularly for initial post-launch and routine periodic calibrations, with discrepancies of only 1.13 s in pointing angle and 2 cm in range correction. Post-calibration verification using ground control points confirmed height measurement accuracy within 0.15 m.

In summary, this calibration method represents a significant improvement over traditional practices, offering a resource-efficient and accurate solution for the geometric calibration of laser altimetry satellites. Its ease of implementation, cost-effectiveness, and versatility make it a powerful tool for frequent and precise on-orbit calibration of laser altimeters.

Author Contributions: Conceptualization, C.X. and J.X.; formal analysis, C.X.; methodology, C.X.; software, C.X. and. Z.W.; validation, C.X. and Z.W.; data curation, F.M. and X.Y.; writing—original draft preparation, C.X.; writing—review and editing, J.X.; visualization, F.M. and X.Y.; supervision, X.W. and J.X. All authors have read and agreed to the published version of the manuscript.

Funding: This work was partly supported by the National Natural Science Foundation of China (No. 42371391).

Data Availability Statement: The GF-7 satellite laser data are available on the Natural Resources Satellite Remote Sensing Cloud Service Platform (http://sasclouds.com/chinese/normal/, accessed on 19 December 2023).

Conflicts of Interest: The authors declare no conflicts of interest.

References

1. Zhang, Z.; Xie, H.; Tong, X.; Zhang, H.; Liu, Y.; Li, B. Denoising for Satellite Laser Altimetry Full-Waveform Data Based on EMD-Hurst Analysis. *Int. J. Digit. Earth* **2020**, *13*, 1212–1229. [CrossRef]
2. Li, B.; Xie, H.; Tong, X.; Tang, H.; Liu, S.; Jin, Y.; Wang, C.; Ye, Z. High-Accuracy Laser Altimetry Global Elevation Control Point Dataset for Satellite Topographic Mapping. *IEEE Trans. Geosci. Remote Sens.* **2022**, *60*, 1–16. [CrossRef]
3. Guo, X.; Jin, S.; Zhang, Z. Evaluation of Water Level Estimation in the Upper Yangtze River from ICESat-2 Data. In Proceedings of the 2021 Photonics & Electromagnetics Research Symposium (PIERS), Hangzhou, China, 21–25 November 2021; pp. 2260–2264.
4. Neumann, T.; Magruder, L.; Kurtz, N. ICESat-2 Mission: Contributions of a Spaceborne Lidar to Ocean Science. In Proceedings of the OCEANS 2022, Hampton Roads, VA, USA, 17–20 October 2022; pp. 1–5.
5. Zhang, S.; Tong, G.; Zhu, C.; Li, J.; Li, X.; Zhu, B.; Liu, L.; Feng, X. Arctic Sea Ice Freeboard Estimation and Variations from Operation IceBridge. *IEEE Trans. Geosci. Remote Sens.* **2022**, *60*, 1–10. [CrossRef]
6. Lu, X.; Yang, Y.; Hu, Y.; Rogers, L.; Omar, A. Global Ocean Studies from ICESat-2 Mission. In Proceedings of the OCEANS 2022, Hampton Roads, VA, USA, 17–20 October 2022; pp. 1–5.
7. Luthcke, S.B.; Thomas, T.C.; Pennington, T.A.; Rebold, T.W.; Nicholas, J.B.; Rowlands, D.D. ICESat-2 Pointing Calibration and Geolocation Performance. *Earth Space Sci.* **2021**, *8*, e2020EA001494. [CrossRef]
8. Steinbrügge, G.; Haynes, M.S.; Schroeder, D.M.; Scanlan, K.M.; Stark, A.; Young, D.A.; Grima, C.; Kempf, S.; Ng, G.; Buhl, D.; et al. Altimetry Measurements from Planetary Radar Sounders and Application to SHARAD on Mars. *IEEE Trans. Geosci. Remote Sens.* **2022**, *60*, 1–14. [CrossRef]
9. Magruder, L.A.; Schutz, B.E.; Silverberg, E.C. Pointing Angle and Timing Calibration/Validation of the Geo-science Laser Altimeter with a Ground-Based Detection System. In Proceedings of the IGARSS 2001. Scanning the Present and Resolving the Future. Proceedings. IEEE 2001 International Geoscience and Remote Sensing Symposium (Cat. No.01CH37217), Sydney, NSW, Australia, 9–13 July 2001; Volume 4, pp. 1584–1587.
10. Xie, J.; Tang, X.; Mo, F.; Tang, H.; Wang, Z.; Wang, X.; Liu, Y.; Tian, S.; Liu, R.; Xia, X. In-Orbit Geometric Calibration and Experimental Verification of the ZY3-02 Laser Altimeter. *Photogramm. Rec.* **2018**, *33*, 341–362. [CrossRef]
11. Tang, X.; Xie, J.; Mo, F.; Dou, X.; Li, X.; Li, S.; Li, S.; Huang, G.; Fu, X.; Liu, R.; et al. GF-7 dual-beam laser altimeter on-orbit geometric calibration and test verification. *Acta Geod. Cartogr. Sin.* **2021**, *50*, 384–395.
12. Xie, J.; Liu, R.; Mo, F.; Tang, H.; Jiao, H.; Mei, Y.; Yang, C. Pointing Bias Calibration of GaoFen-7 Laser Altimeter Based on Single Laser Footprint Image. *ISPRS Ann. Photogramm. Remote Sens. Spat. Inf. Sci.* **2020**, *2*, 113–119. [CrossRef]
13. Luthcke, S.B.; Carabajal, C.C.; Rowlands, D.D. Enhanced Geolocation of Spaceborne Laser Altimeter Surface Returns: Parameter Calibration from the Simultaneous Reduction of Altimeter Range and Navigation Tracking Data. *J. Geodyn.* **2002**, *34*, 447–475. [CrossRef]
14. Luthcke, S.B.; Rowlands, D.D.; McCarthy, J.J.; Pavlis, D.E.; Stoneking, E. Spaceborne Laser-Altimeter-Pointing Bias Calibration from Range Residual Analysis. *J. Spacecr. Rocket.* **2000**, *37*, 374–384. [CrossRef]
15. Luthcke, S.B.; Rowlands, D.D.; Williams, T.A.; Sirota, M. Reduction of ICESat Systematic Geolocation Errors and the Impact on Ice Sheet Elevation Change Detection. *Geophys. Res. Lett.* **2005**, *32*, L21S01. [CrossRef]
16. Liu, R.; Xie, J. Calibration of the Laser Pointing Bias of the GaoFen-7 Satellite Based on Simulation Waveform Matching. *Opt. Express* **2021**, *29*, 21844–21858. [CrossRef] [PubMed]
17. Li, S.; Yu, Q.; Fu, A.; Zhang, G. A Calibration Method for Large-Footprint Full-Waveform Airborne Laser Altimeter without a Calibration Field. *Remote Sens.* **2023**, *15*, 2789. [CrossRef]
18. Tang, X.; Xie, J.; Gao, X.; Mo, F.; Feng, W.; Liu, R. The In-Orbit Calibration Method Based on Terrain Matching with Pyramid-Search for the Spaceborne Laser Altimeter. *IEEE J. Sel. Top. Appl. Earth Obs. Remote Sens.* **2019**, *12*, 1053–1062. [CrossRef]

19. Xie, J.; Mo, F.; Feng, W.; Liu, R. The On-Orbit Calibration Method Based on Terrain Matching with Pyramid-Search for the Spaceborne Laser Altimeter. In Proceedings of the IGARSS 2018—2018 IEEE International Geoscience and Remote Sensing Symposium, Valencia, Spain, 22–27 July 2018; pp. 1978–1981.
20. Zhao, P.; Li, S.; Ma, Y.; Liu, X.; Yang, J.; Yu, D. A New Terrain Matching Method for Estimating Laser Pointing and Ranging Systematic Biases for Spaceborne Photon-Counting Laser Altimeters. *ISPRS J. Photogram. Remote Sens.* **2022**, *188*, 220–236. [CrossRef]
21. Liu, R.; Xie, J.; Xu, C.; Zeng, J.; Mo, F.; Yang, X. A Separate Calibration Method of Laser Pointing and Ranging for the GF-7 Satellite Laser That Does Not Require Field Detectors. *Remote Sens.* **2022**, *14*, 5935. [CrossRef]
22. Xie, J.; Liu, R.; Yang, X.; Mo, F.; Zhang, F.; Liu, L. On-Orbit Geometric Calibration of Satellite Laser Altimeters Using Infrared Detectors and Corner-Cube Retroreflectors. *Int. J. Digit. Earth* **2023**, *16*, 2067–2088. [CrossRef]
23. Zhou, P.; Tang, X.M. Geometric Accuracy Verification of GF-7 Satellite Stereo Imagery without GCPs. *IEEE Geosci. Remote Sens. Lett.* **2022**, *19*, 1–5. [CrossRef]
24. Tang, X.; Liu, C.; Zhang, H.; Wang, X.; Li, G.; Mo, F.; Li, F. GF-7 Satellite Stereo Images Block Adjustment Assisted with Laser Altimetry Data. *Geomat. Inf. Sci. Wuhan Univ.* **2021**, *46*, 1423–1430.
25. Xie, J.; Huang, G.; Liu, R.; Zhao, C.; Dai, J.; Jin, T.; Mo, F.; Zhen, Y.; Xi, S.; Tang, H.; et al. Design and Data Processing of China's First Spaceborne Laser Altimeter System for Earth Observation: GaoFen-7. *IEEE J. Sel. Top. Appl. Earth Obs. Remote Sens.* **2022**, *13*, 1034–1044. [CrossRef]
26. Du, L.; Pang, Y.; Ni, W.; Liang, X.; Li, Z.; Suarez, J.; Wei, W. Forest Terrain and Canopy Height Estimation Using Stereo Images and Spaceborne LiDAR Data from GF-7 Satellite. *Geo-Spat. Inf. Sci.* **2023**, 1–11. [CrossRef]
27. Tang, X.; Xie, J.; Liu, R.; Huang, G.; Zhao, C.; Zhen, Y.; Tang, H.; Dou, X. Overview of the GF-7 Laser Altimeter System Mission. *Earth Space Sci.* **2020**, *7*, e2019EA000777. [CrossRef]
28. Hou, P.Y.; Zha, J.P.; Liu, T.; Zhang, B.C. Recent advances and perspectives in GNSS PPP-RTK. *Meas. Sci. Technol.* **2023**, *34*. [CrossRef]
29. Schenk, T.; Csatho, B.; Neumann, T. Assessment of ICESat-2's Horizontal Accuracy Using Precisely Surveyed Terrains in McMurdo Dry Valleys, Antarctica. *IEEE Trans. Geosci. Remote Sens.* **2022**, *60*, 4303811. [CrossRef]
30. Abdalati, W.; Zwally, H.J.; Bindschadler, R.; Csatho, B.; Farrell, S.L.; Fricker, H.A.; Harding, D.; Kwok, R.; Lefsky, M.; Markus, T.; et al. The ICESat-2 Laser Altimetry Mission. *Proc. IEEE* **2010**, *98*, 735–751. [CrossRef]
31. Wang, C.; Yang, X.B.; Xi, X.H.; Zhang, H.B.; Chen, S.C.; Peng, S.W.; Zhu, X.X. Evaluation of Footprint Horizontal Geolocation Accuracy of Spaceborne Full-Waveform LiDAR Based on Digital Surface Model. *IEEE J. Sel. Top. Appl. Earth Obs. Remote Sens.* **2020**, *13*, 2135–2144. [CrossRef]
32. Gribov, A.; Krivoruchko, K. Empirical Bayesian Kriging Implementation and Usage. *Sci. Total Environ.* **2020**, *722*, 137290. [CrossRef]
33. Biernacik, P.; Kazimierski, W.; Włodarczyk-Sielicka, M. Comparative Analysis of Selected Geostatistical Methods for Bottom Surface Modeling. *Sensors* **2023**, *23*, 3941. [CrossRef]
34. Krivoruchko, K.; Gribov, A. Evaluation of Empirical Bayesian Kriging. *Spat. Stat.* **2019**, *32*, 100368. [CrossRef]
35. Krivoruchko, K.; Gribov, A. Distance Metrics for Data Interpolation over Large Areas on Earth's Surface. *Spat. Stat.* **2020**, *35*, 100396. [CrossRef]
36. Krivoruchko, K.; Gribov, A. Pragmatic Bayesian Kriging for Non-Stationary and Moderately Non-Gaussian Data. In *Mathematics of Planet Earth: Proceedings of the 15th Annual Conference of the International Association for Mathematical Geosciences*; Springer: Cham, Switzerland, 2014; pp. 61–64.
37. Novaczek, E.; Devillers, R.; Edinger, E. Generating Higher Resolution Regional Seafloor Maps from Crowd-Sourced Bathymetry. *PLoS ONE* **2019**, *14*, e0216792. [CrossRef] [PubMed]
38. Yang, X.; Xie, J.; Liu, R.; Mo, F.; Zeng, J. Centroid Extraction of Laser Spots Captured by Infrared Detectors Combining Laser Footprint Images and Detector Observation Data. *Remote Sens.* **2023**, *15*, 2129. [CrossRef]
39. Xie, H.; Li, B.B.; Tong, X.H.; Zhang, X.W.; He, T.; Dai, J.; Huang, G.H.; Zhang, Z.J.; Liu, S.J. A Planimetric Location Method for Laser Footprints of the Chinese GaoFen-7 Satellite Using Laser Spot Center Detection and Image Matching to Stereo Image Product. *IEEE Trans. Geosci. Remote Sens.* **2021**, *59*, 9758–9771. [CrossRef]